Description and validation of the Japanese algorithm for radiative flux and heating rate products with all four EarthCARE instruments : Pre-launch test with A-Train

Akira Yamauchi[1], Kentaroh Suzuki[1], Eiji Oikawa[2], Miho Sekiguchi[3], Takashi M. Nagao[1], Haruma Ishida[4]

5 [1]Atmosphere and Ocean Research Institute, University of Tokyo, Kashiwa, Japan
[2]Meteorological Research Institute, Japan Meteorological Agency, Tsukuba, Japan
[3]Faculty of Marine Technology, Tokyo University of Marine Science and Technology, Tokyo, Japan
[4]Meteorological Satellite Center, Japan Meteorological Agency, Tokyo, Japan

Correspondence to: Akira Yamauchi (ayamauchi@g.ecc.u-tokyo.ac.jp)

10   **Abstract.** This study developed the Level 2 (L2) atmospheric radiation flux and heating rate product by a Japanese team for Earth Cloud, Aerosol, and Radiation Explorer (EarthCARE). This product offers vertical profiles of downward and upward longwave (LW) and shortwave (SW) radiative fluxes and their atmospheric heating rates. This paper describes the algorithm developed for generating products, including the atmospheric radiative transfer model and input datasets, and its validation against measurement data of radiative fluxes. In the testing phase before the EarthCARE launch, we utilized A-Train data that

15 provided input and output variables analogous to EarthCARE, so that the developed algorithm could be directly applied to EarthCARE after its launch. The aerosol and cloud vertical profile data obtained from the CloudSat/CALIPSO/MODIS satellites were used as major input to perform the radiative transfer simulations. The results include comparisons of radiative fluxes between radiative transfer simulations and satellite/ground-based observations that quantify errors in computed radiative fluxes at the top of the atmosphere against Clouds and Earth's Radiant Energy System (CERES) observations and their

20 dependence on cloud type with varying thermodynamic phases. For SW fluxes, the bias was 24.4 Wm^{-2}, and the root mean square error (RMSE) was 36.3 Wm^{-2} relative to the CERES observations at spatial and temporal scales of 5 °and 1 month, respectively. On the other hand, LW exhibits a bias of -10.7 Wm^{-2} and an RMSE of 14.2 Wm^{-2}. When considering different cloud phases, the SW water cloud exhibited a bias of -11.7 Wm^{-2} and an RMSE of 46.2 Wm^{-2}, while the LW showed a bias of 0.8 Wm^{-2} and an RMSE of 6.0 Wm^{-2}. When ice clouds were included, the SW bias ranged from 58.7 to 81.5 Wm^{-2} and the

25 RMSE from 72.8 to 91.6 Wm^{-2} depending on the ice-containing cloud types, while the corresponding LW bias ranged from -8.8 to -28.4 Wm^{-2} and the RMSE from 25.9 to 31.8 Wm^{-2}, indicating that the primary source of error was ice-containing clouds. The comparisons were further extended to various spatiotemporal scales to investigate the scale dependency of the flux errors. The SW component of this product exhibited an RMSE of approximately 30 Wm^{-2} at spatial and temporal scales of 40 °and 40 days, respectively, whereas the LW component did not show a significant decrease in RMSE with increasing

30 spatiotemporal scale. Radiative transfer simulations were also compared with ground-based observations of the surface

downward SW and LW radiative fluxes at selected locations. The results show that the bias and RMSE for SW are -17.6 Wm^{-2} and 172.0 Wm^{-2}, respectively, which are larger than those for LW that are -5.6 Wm^{-2} and 19.0 Wm^{-2}, respectively.

1. Introduction

35   Clouds and aerosols play a significant role in shaping the Earth's radiation budget, exerting a substantial influence on global climate. Changes in the planet's radiation balance can affect atmospheric circulation patterns (Hartmann and Short, 1980; Liebmann and Hartmann, 1982). In particular, the energy imbalances caused by aerosols and clouds, quantified by their radiative forcing, can affect atmospheric circulation and the transport of water vapor. However, their quantitative estimates are still subject to significant uncertainty. The commencement of observations by the Earth Radiation Budget (ERB) onboard

40   NIMBUS-7 in 1978 marked an improvement in our understanding of the radiation budget at the top of the atmosphere (TOA) (Kyle et al., 1985). With the launch of the Earth Radiation Budget Experiment (ERBE) in 1984, observations of the radiation budget at the TOA became more precise (Barkstrom, 1984). Broadband radiometer observations at the TOA have continued since then and now provide valuable long-term data through instruments such as the Earth's Radiant Energy System (CERES, Wielicki et al.1996). Observations conducted by the broadband radiometer at the TOA were utilized to ascertain the Earth's

45   overall energy budget. The radiation budget estimate is important not only at the TOA but also at the atmosphere (ATM) and surface (SFC) to quantify the energy partitioning into ATM and SFC, with implications for climate effects due to their differing heat capacities. Although radiation fluxes at the TOA can be directly observed by the broadband radiometer, observing fluxes at the ATM and SFC is more challenging. Typically, fluxes at the ATM and SFC are estimated using radiative transfer (RT) computations utilizing aerosol and cloud parameters obtained from various satellites as inputs.

50   Information about clouds and aerosols obtained from passive sensors has been utilized in RT computations to estimate the Earth's energy budget (e.g., Fasullo and Trenberth, 2008a, b). However, passive sensors do not provide vertical profile information, resulting in significant uncertainty in the estimation of the cloud base height, which particularly influences the longwave (LW) radiative flux. CloudSat (Stephens et al. 2008) and the Cloud–Aerosol lidar and Infrared Pathfinder Satellite Observations (CALIPSO; Winker et al. 2010) satellites were introduced to the A-Train satellite constellation and provided

55   crucial vertical profile information about clouds and aerosols. The downward longwave radiation at the surface estimated by using the cloud vertical distributions observed by CloudSat and CALIPSO was found to be 10 Wm^{-2} larger than model-based estimations in the decade of 2000s (Stephens et al., 2012). Recent studies have indicated that Earth's radiation budget is affected by the vertical distribution of clouds (Li et al., 2015; Oreopoulos et al., 2017), emphasizing the importance of understanding the vertical distribution of clouds. This improved understanding was achieved with atmospheric radiation products generated

60   from the CloudSat/CALIPSO cloud and aerosol vertical information, such as 2B-FLXHR and 2B-FLXHR-Lidar (L'Ecuyer et al., 2008; Henderson et al., 2013) developed by NASA's CloudSat team, and Clouds and CERES-CALIPSO-CloudSat- Moderate-Resolution Imaging Spectroradiometer (MODIS) (CCCM, Kato et al., 2011) developed by the CERES team. The accuracy of these products based on active sensors was verified through comparisons with ground- and satellite-based observations of radiative fluxes at the TOA and surface (L'Ecuyer et al., 2008). The Earth Cloud, Aerosol, and Radiation

65 Explorer (EarthCARE) satellite, scheduled for launch in 2024 as a "successor" to the CloudSat/CALIPSO satellites, will provide even more detailed information on cloud and aerosol vertical distributions, particularly with Doppler capability of measuring vertical motion of cloud particles (Illingworth et al., 2015). Novel EarthCARE information is expected to offer even more accurate pictures of Earth's energy budget in conjunction with cloud dynamics.

To this end, Japanese and European teams are independently developing aerosol, cloud, and radiation products for the
70 EarthCARE satellite mission, which will become available to the research community after its launch. This study describes an algorithm developed for generating one of the products offered by the Japanese team, namely the Level 2 (L2) atmospheric radiative flux and heating rate product listed in Kikuchi et al., (2019), including aerosol and cloud radiative forcings, and its validation against satellite- and ground-based measurements of radiative fluxes at the top of the atmosphere and at the surface. This product was generated using cloud and aerosol vertical profile information from the EarthCARE satellite instruments
75 of Cloud Profiling Radar (CPR), ATmospheric Lidar (ATLID), and multi-spectral imager (MSI), and was validated against measurements of radiative fluxes from the Broadband Radiometer (BBR) also onboard EarthCARE. The L2 atmospheric radiative flux and heating rate product provides vertical profiles of the downward and upward radiative fluxes for LW and SW and their respective atmospheric heating rates. When employed alongside other Japanese L2 cloud and aerosol products, it is possible to discern the impact of various cloud and aerosol characteristics, particularly in their vertical dimensions, on
80 atmospheric radiation. A European team is currently developing an equivalent atmospheric radiation product (Cole et al., 2023). Once the data are released, cross comparisons with our dataset will be conducted to evaluate the products and enhance their accuracy. These products serve as fundamental data for a variety of climate research applications, including the evaluation and improvement of global climate models. The objective of this study was to develop and validate the accuracy of the Japanese team's L2 atmospheric radiation algorithm and characterize the source of radiative flux errors when applied to real observed
85 satellite measurement data. One particular criteria to be used for evaluating the EarthCARE science goals is whether the error between RT flux and observations remains within ±10 Wm^{-2}. To provide fundamental information for such an assessment and broader scientific data use, it is important to investigate the extent to which the flux error varies with spatiotemporal scales. To this end, this study quantified the flux errors at various spatiotemporal scales.

In the testing phase, before the launch of EarthCARE, we utilized A-Train-based aerosol and cloud vertical profile data
90 obtained from the CloudSat/CALIPSO/MODIS satellites, which provided data analogous to those expected from EarthCARE, as input data. This served as a preliminary evaluation prior to the official launch of EarthCARE. Knowledge of the aerosol type is crucial for assessing the aerosol radiative effect. In this regard, it is worth noting that the types of aerosols characterized may vary between A-Train and EarthCARE products. For instance, the number of aerosol types in the post-EarthCARE launch product has increased from three (water-soluble (WS), dust (DS), and sea salt (SS)) to four, incorporating WS, light-absorbing
95 (LA), DS, and SS (Nishizawa et al., 2007, 2008, 2011, 2019; Kudo et al. 2023). The post-launch EarthCARE product incorporates four aerosol species into the radiative transfer calculations to generate radiative fluxes and aerosol radiative effects due to the four aerosol species.

The remainder of this paper is organized as follows. Section 2 describes the atmospheric radiative transfer model, input dataset, and validation data. In Section 3, we present validation results by comparing our atmospheric radiation products with those from NASA in terms of flux errors relative to the CERES measurements of radiative fluxes at the TOA. The comparison is shown in the form of the spatiotemporal scale dependency of the flux errors and error characteristics broken down into different cloud types with varying thermodynamic phases on a global scale. In Section 4, the radiative fluxes are validated at the ground surface and the errors between the fluxes of this product and the ground-based fluxes of the Baseline Surface Radiation Network (BSRN) are presented. In Section 5, the radiative forcings of clouds and aerosols are estimated based on the validated radiative fluxes to demonstrate how the radiative effects of aerosols and clouds can be quantified using this product. Finally, Section 6 summarizes the conclusions of this study.

2. Data and Methods

The radiative flux of this product was obtained through vertical one-dimensional radiative transfer calculations utilizing information on the vertical profiles of aerosols and clouds along with meteorological data as input. During the pre-launch test phase, the A-train satellite constellation was used as a substitute for EarthCARE. Aerosol vertical profile data from the CALIPSO satellite and cloud vertical profile data from CloudSat/CALIPSO/MODIS were used for this purpose. After the launch of EarthCARE, aerosol profile data obtained from ATLID and cloud profile data acquired from CPR/ATLID/MSI were utilized. This product offers SW and LW radiative fluxes, their respective radiative heating rates, and the radiative forcing of clouds and aerosols. The accuracy of this product was validated by comparing radiative fluxes with those measured by available satellite instruments (CERES in A-Train and BBR in EarthCARE) at the TOA and with those obtained from BSRN at the surface. In the next section, the details of the input data and radiative transfer model used are described.

2.1 Input Data and radiative transfer model

Input data for aerosols were obtained from the Japan Aerospace Exploration Agency (JAXA) LIDAR Aerosol Property Product (CA-Aprop) (Nishizawa et al., 2007, 2008, 2011). This product employs the attenuated backscatter coefficients at 532 and 1064 nm as well as the depolarization ratio at 532 nm observed by CALIPSO lidar, to derive the vertical profiles of three aerosol types: water-soluble aerosols (a mixture of sulfate, nitrate, and organic aerosols), dust, and sea salt.

The input data for ice clouds were obtained from JAXA's Radar/Lidar Cloud Microphysics Property Product (CSCA-Micro) (Okamoto et al., 2010; Sato and Okamoto, 2011), which provides information on the ice particle effective radius and Ice Water Content (IWC). The input data for the water clouds, that is, the liquid particle effective radius and Cloud Water Content (CWC), were obtained from NASA's CloudSat 2B-CWC-RO-R04 product (Austin et al., 2009). NASA's product was used in our current developmental version of the algorithm because of the lack of a long-term CWC dataset in the current version of the JAXA CSCA-Micro product. However, it will be replaced by JAXA's CWC in the operational product after EarthCARE is launched.

The total cloud optical thickness (COT) was also used to better constrain cloud radiative properties, particularly for SW. The COT data were obtained from JAXA's Moderate Resolution Imaging Spectrometer (MODIS) Imager Cloud Property Product (MOD-Micro, Nakajima and Nakajima 1995; Nakajima et al., 2019; Wang et al., 2023). Voronoi particles (Ishimoto et al., 2010) were assumed in the COT retrieval of ice clouds from MODIS. In cases where the MODIS COT was available, the

135 extinction coefficient for each vertical layer originally derived from the CloudSat/CALIPSO was rescaled by the total COT derived from MODIS. When the COT was not available from MODIS, the extinction coefficient derived from the CloudSat/CALIPSO data was used directly. The meteorological field variables (pressure, temperature, and specific humidity) required for the radiative transfer calculations were obtained from NASA's Goddard Earth Observing System (GEOS-4, 5) Data Assimilation System (Bloom et al., 2005; Rienecker et al., 2008). The ground surface albedo data used in this study were

140 obtained from the MODIS global albedo product, MCD43C3 (Roesch et al., 2004; Schaaf et al., 2002). Sea surface albedo was set to 0.05.

All input data, including aerosol and cloud profiles, meteorological field variables, and ground surface albedo, were averaged to a horizontal resolution of 5 km and 34 vertical layers prior to their use in the radiative transfer calculations. Radiative transfer simulations were performed using the one-dimensional plane-parallel radiative transfer (RT) model of MstrnX

145 (Sekiguchi and Nakajima, 2008; Nakajima et al., 2000) that is based on the delta two-stream discrete ordinate method with a k-distribution approximation for gaseous absorptions. The MstrnX used in this study discretizes whole the spectrum into 29 spectral bands for radiative transfer calculations, including 15 solar bands and 14 thermal bands. These calculations rely on gas absorption data tables based on HITRAN2004 (Rothman et al., 2005), encompassing major gaseous constituents such as H_2O, CO_2, O_3, N_2O, CO, CH_4, and O_2. Reanalysis data of temperature, pressure, specific humidity, and O_3 were also utilized

150 for the gaseous calculations in the model. As an assumption of the ice cloud optical properties, Voronoi particles (Ishimoto et al., 2010) were used to account for the non-spherical shape of the ice particles. This assumption of ice particles in the RT simulation was consistent with that of the MODIS ice cloud retrievals.

The results for the radiative fluxes obtained from the radiative transfer calculations were compared with data from the CERES measurements at the TOA, the Baseline Surface Radiation Network (BSRN, Ohmura et al., 1998) measurements at

155 the surface, and the CloudSat/CALIPSO 2B-FLXHR-Lidar products of versions R04 and R05 (L'Ecuyer et al., 2008; Henderson et al., 2013) at the TOA for validation. In line with both this product and other NASA flux products, only the diurnal flux data were utilized for the four-month comparison period of January, April, July, and October, 2007. The presence of aerosols and clouds can significantly influence radiation calculations and requires verification under various conditions. Therefore, this study compared all-sky conditions, including all clouds observed, and cloudy conditions of different types with

160 varying cloud phases. Under all-sky conditions, comparisons were made even when data were available only from CloudSat/CALIPSO (not from MODIS) to maximize cloud samples with vertical profiles. However, for cloud-type classification using the thermodynamic phase, only cases with available MODIS data were considered for comparison. For comparison with 2B-FLXHR-Lidar regarding different cloud types, the 2B-CLDCLASS-Lidar R05 (Sassen et al., 2008) and MOD06-1KM-AUX R05 (Platnick et al., 2017) products were used for cloud type classification. To ensure a consistent

165 comparison between the RT simulations and CERES measurements, the simulated radiative fluxes were averaged over a 20 km area to match the CERES footprint. When comparing with BSRN, the surface measurement time closest to the CloudSat transit time within ±0.1 deg of the footprint was selected. The time was matched such that the time difference between the A-Train transit and ground observation was no more than 10 min at maximum.

To quantify the flux errors of the RT simulations against observations, the bias and Root-Mean Square Error (RMSE)
170 relative to observations were calculated as follows:

$$\text{Bias} = \frac{1}{n}\sum_{i=1}^{1}[(\text{FLUX}_{\text{RT}})_i - (\text{FLUX}_{\text{obs}})_i] \,, \tag{1}$$

$$\text{RMSE} = \left[\frac{1}{n}\sum_{i=1}^{1}[(\text{FLUX}_{\text{RT}})_i - (\text{FLUX}_{\text{obs}})_i]^2\right]^{1/2} \,, \tag{2}$$

where FLUX_{RT} denotes the radiative flux calculated by the RT model, and FLUX_{obs} denotes the observed flux value. The fluxes are then converted into radiative heating rate using the following equation:

175
$$\frac{dT}{dt} = \frac{g}{C_p}\frac{dF}{dp} \,, \tag{3}$$

where T is the temperature (K), t is time (s), g is the acceleration due to gravity (m s^{-2}), C_p is the specific heat content of air at constant pressure (J kg^{-1} K^{-1}), F is the radiative flux (W m^{-2}), and p is the pressure (Pa).

3 Comparison with CERES observation at TOA

The radiative flux products were validated by comparing them with CERES observations at the TOA, which have a footprint
180 of approximately 20 km, whereas CloudSat/CALIPSO provides information along a 1.1 km nadir path, making it difficult to make a perfectly consistent comparison. However, it is crucial to estimate errors through comparisons with observations, even when considering this discrepancy on a spatial scale. In this study, the results of the RT calculations were averaged over 20 km to closely match the CERES observations. In this section, a comparison between this product and CERES observations at the TOA is presented, and the verification and limitations of the errors under various cloud conditions are described and
185 discussed. Section 3.1 exemplifies the vertical profiles of aerosols and clouds as crucial inputs to the current algorithm, along with the results of radiative transfer calculations and comparisons with flux measurements. This section illustrates how aerosols and clouds can influence radiative transfer calculations, and how their measurement uncertainty can introduce radiative flux errors. In Section 3.2, the radiative fluxes between the RT simulations and observations are compared as monthly averages with a horizontal resolution of 5° to quantify the global bias and RMSE. The validity of this product was further confirmed by
190 comparison with the radiation flux product developed by the NASA CloudSat/CALIPSO team. The radiative flux comparisons were then broken down into different thermodynamic phases of clouds, a factor that significantly impacts the radiative fluxes. Given that the flux error characteristics vary with the spatiotemporal scales, on which the assessment of aerosol and cloud radiative effects depends, the RMSE values were also investigated by altering the spatiotemporal scales (Section 3.3) to quantify the scale dependence of the RMSE in this algorithm.

3.1 Demonstration of input and output

To demonstrate how the algorithm works to produce radiative fluxes and heating rates with major inputs of aerosols and clouds, an example of the RT calculation with clouds and aerosols in an orbital element is provided, highlighting the conditions that can cause flux errors. Figure 1 shows a comparison of the radiative fluxes at the TOA between a radiative transfer calculation and the observed value. Figure 1(a) shows the cloud phase of MODIS observation along with the A-Train satellite orbit and Figure 1(b) and 1(c) show the vertical profiles of the aerosols and clouds used as inputs of the RT model. The computed radiative flux was subsequently used to determine the radiative heating profile (Figure 1(d)). The accuracy of the radiative fluxes and radiative heating rates was verified through a comparison with observations at the TOA. Figure 1(e) compares the calculated and CERES-observed fluxes for LW and SW radiation. The LW radiation was generally consistent with the observations, regardless of the cloud or aerosol distribution. However, SW radiation shows a greater discrepancy from the observations, particularly when clouds are present. This greater discrepancy in the presence of clouds is likely attributable to the significant influence of cloud optical properties and their dependence on the thermodynamic phase used as the input information. In the subsequent sections, we present a comparison of our RT simulations and other products with CERES measurements on a global scale and their classification into cloud thermodynamic phases to investigate the flux errors of our product in more detail.

3.2 Global validation and effects of cloud phase

In this section, radiative flux errors against CERES measurements are investigated on a global scale under different atmospheric conditions to assess the sources of flux errors in more detail. First, the global validation results are shown in the form of bias relative to CERES observations for both our product and NASA's product under all-sky conditions. Figure 2 shows comparisons between the calculated SW and LW radiative fluxes at the TOA and those from CERES observations at a spatial scale of 5 ° and a temporal scale of 1 month. The SW flux in this study is positively biased relative to CERES (Figure 2(a)), and the positive bias of 24.4 Wm^{-2} is somewhat larger than that of 2B-FLXHR-Lidar R04/R05 (-1.2 Wm^{-2} and -2.1 Wm^{-2}; Figure 2 (b)-(c)). However, the RMSE of this study (36.3 Wm^{-2}) is smaller than that of 2B-FLXHR-Lidar R04 (46.4 Wm^{-2}), indicating that the results of this study have less variability relative to CERES than does 2B-FLXHR-Lidar R04. Although our product shows a positive bias, the RMSE minus the bias, representing the variability component of the RMSE, tends to be smaller than that of the other products, as illustrated by the smaller scatter in Figure 2(a) compared to Figures. 2(b) and 2(c). However, the LW fluxes in this study showed similar accuracy in terms of bias and RMSE as 2B-FLXHR-Lidar R04/R05 (Figure 2 (d)–(f)). Possible sources of positive bias in the SW flux can be attributed to flux errors found under a particular cloud thermodynamic phase condition, as discussed below.

The cloud thermodynamic phase has a significant impact on radiation; thus, its measurement uncertainty and treatment in RT simulations can introduce errors into the estimated radiative fluxes. Therefore, it is useful to classify the global flux

comparisons described above into different cloud phases to assess the flux errors and identify the factors contributing to these errors. For this purpose, this study exploited cloud thermodynamic phase information obtained from CloudSat/CALIPSO (CC) and MODIS (MOD) to classify scenes into different cloud phase categories. Based on the phase characterization by CC, "Water"

230 and "Ice" are defined such that all the vertical layers were composed of water (liquid) clouds and ice clouds, respectively, and "Mixed" is defined as a mixture of ice and water within the vertical profile. For single-layered clouds, these CC-based phase discriminations are combined with MOD-based binary phase discriminations of "Water" and "Ice" to produce the four phase categories of "Water/Water", "Water/Ice", "Ice/Water", and "Mixed" in the order of CC/MOD for the first three categories. The multi layered clouds as observed by CC, which are difficult to observe by MODIS (MOD), are categorized separately as

235 "Multi," and the discrimination between "Mixed" and "Multi" is based on the cloud phase information obtained from CC.

Figure 3 shows a breakdown of the comparison in Figure 2 according to cloud type with the different cloud phase conditions described above. Specifically, Figures 3(a)–(d) and (f)–(i) show comparisons of single-layer clouds for the SW and LW fluxes, respectively, with varying cloud-phase characterizations by CC and MOD, while Figures 3(e) and (j) show comparisons of multi-layer clouds for the SW and LW fluxes, respectively. To reduce flux errors arising from horizontal cloud heterogeneity,

240 comparisons were performed only when clouds within the CERES footprint were of the same cloud type. When both CC and MOD indicate water clouds, the SW flux shows a slight negative bias, but both the bias (-11.7 Wm^{-2}) and RMSE (46.2 Wm^{-2}) are relatively small (Figure 3(a)). On the other hand, the LW flux shows no substantial bias (0.8 Wm^{-2}) and a small RMSE (6.0 Wm^{-2}) (Figure 3(f)). However, when ice clouds were included in the CC, the SW flux exhibited a positive bias and both the bias and RMSE were larger (Figure 3(b)–(d)). Additionally, the LW flux exhibited a negative bias (Figure 3 (g)–(i)). The

245 positive SW bias could have been caused by a possible overestimation of the ice cloud optical thickness obtained from MODIS, particularly with the assumption of Voronoi-type ice particles that enhance backscatter. The positive bias was significantly reduced when the RT calculation was performed with a 30% reduction in the ice cloud optical thickness, highlighting the key role of the ice cloud optical properties in determining the SW flux. It was also confirmed that the positive bias was reduced when the RT calculation was performed by replacing the MODIS COT with the NASA product of MAC06S0 (not shown).

250 The negative bias observed in the LW for ice-containing clouds may be due to an overestimation of the cloud-top height obtained from the CC or an underestimation of the cloud-top temperature calculated by using the reanalysis data. The EarthCARE satellite is expected to reduce the LW bias by providing more accurate cloud detection through improved measurement instrumentation. The same bias occurs in the case of Multi as in the case of ice-containing clouds, which can be understood by the tendency for Multi to also contain a significant number of ice clouds, such as upper-level cirrus clouds.

255

3.3 Scale dependence of the flux error

Given the spatiotemporal scale dependence of radiative fluxes, validation of RT-simulated fluxes against measurements needs to be performed over different spatial and temporal scales. Such scale-dependent validation is also beneficial for product users who may use the data at various spatiotemporal scales depending on their analysis purposes. To this end, the RT-calculated

260   and CERES-measured fluxes were compared at various spatiotemporal scales. Figure 4 shows a comparison of the variation in RMSE as a function of spatial and temporal scales for both all-sky SW and LW radiation fluxes at the TOA. All the results indicated a systematic reduction in the RMSE as the spatiotemporal scale increased. The reduction is more pronounced with changes in the spatial scale than with changes in the temporal scale. This can be attributed to the fact that the A-Train satellite constellation passes over the same location only twice a day, whereas a larger number of samples are available for comparison

265   with observations at larger spatial scales, resulting in a smaller effect on the RMSE with an increasing temporal scale than with an increasing spatial scale.

    The scale dependences of the flux error were also analyzed using the 2B-FLXHR-Lidar products and compared with those of our product, as shown in Figure 4. Compared to 2B-FLXHR-Lidar R04 and R05, this study exhibited lower RMSE values for SW radiative fluxes at lower spatial resolutions (Figure 4 (a)–(c)). At higher spatiotemporal scales, the RMSE was

270   approximately 30 Wm^{-2} at spatial and temporal scales of 40 °and 40 days, which was comparable to that of 2B-FLXHR-Lidar R04. However, for the 2B-FLXHR-Lidar R05 at high spatiotemporal scales, the RMSE decreased to approximately 10 Wm^{-2} in contrast to our product, which had an RMSE of approximately 30 Wm^{-2}. This was attributed to a positive bias in the RT-calculated fluxes in this study relative to the observed values, as discussed in Sections 3.1 and 3.2. Regarding the LW radiation fluxes (Figure 4 (d)–(f)), the RMSE did not significantly decrease as the spatiotemporal scale increased in this study compared

275   to 2B-FLXHR-Lidar R04 and R05. This is consistent with the negative bias of our product when ice clouds are included, as described in Section 3.2.

    The scale dependence of the flux errors is also likely influenced by the cloud phase and type, which significantly influence the bias and RMSE, as demonstrated in Section 3.2. Given that the primary cloud types as sources of flux errors were identified based on the RMSE by classifying the cloud phases, the scale dependence of the flux error was also broken down into different

280   cloud types. Figure 5 shows the RMSE statistics as a function of varying spatiotemporal scales for different cloud-type categories defined in the same manner as in Section 3.2. For the SW water cloud, the RMSE showed a decreasing trend as the spatiotemporal scale increased, reaching approximately 20 Wm^{-2} (Figure 5 (a)). However, when ice clouds were included, the RMSE exceeded 80 Wm^{-2} for smaller spatiotemporal scales, and remained at approximately 70 Wm^{-2} for larger scales (Figure 5 (b)–(e)). Similarly, for LW radiation, the RMSE exhibited a decreasing tendency with increasing spatio-temporal scale in

285   the case of water clouds. However, when ice clouds were included, the RMSE did not show a significant decrease, even at larger spatiotemporal scales. The results from the cloud-type classification appear to explain the relatively small decrease in the all-sky RMSE with increasing spatiotemporal scale in Figure 4 (a) and (d), reflecting the small reduction in RMSE in ice-containing clouds at even larger scales. This suggests that the positive flux bias of ice-containing clouds demonstrated in Section 3.2 tends to exist across a varying range of spatiotemporal scales, consequently yielding a larger RMSE under all-sky

290   conditions.

4. Surface Validation

RT simulations can calculate surface (SFC) fluxes as well as TOA, and validating both TOA and SFC allows for a proper assessment of the impact of clouds and aerosols on atmospheric radiation. The error quantification not only at TOA but also at SFC can also aid in assessing the influence of atmospheric radiation on ATM, enabling to characterize the flux errors in radiative energy partitioning into ATM and SFC. This section quantitatively evaluates the product by comparing instantaneous RT fluxes with ground-based BSRN observations.

Figure 6 compares the downward radiative fluxes calculated using the RT and those observed by the BSRN at the ground surface across different locations. In the comparison of SW radiation fluxes (Figure 6 (a), (c)), a minor bias of -17.6 Wm^{-2} is noted, but the RMSE is substantial at 172.0 Wm^{-2} , with a sample number of 47. The discrepancies in the bias and RMSE values can be attributed to the limited number of samples available for comparison. Furthermore, the flux error may vary considerably depending on the specific measurement location, possibly owing to the potential issue of varying measurement accuracy across different locations under different meteorological conditions, although no significant differences were observed between clear-sky and cloudy-sky conditions. In the comparison of LW radiation flux (Figure 6 (b), (d)), both the bias and RMSE (-5.6 and 19.0 Wm^{-2}) are significantly smaller compared to the SW flux, with a sample number of 44. The different number of samples between SW and LW reflects the variation in number of observation sites where SW and LW measurements are available. Unlike the SW radiation flux, no noticeable differences were observed in the calculated values based on observation location. Additionally, no significant differences were observed between clear- and cloudy-sky conditions for the LW radiation flux. Assuming a scale dependence of the flux error similar to that of the TOA radiative flux described in Section 3, the bias and RMSE against the ground measurements are expected to decrease with increasing sample size. Compared to ground-based observations, CloudSat's narrow footprint of 1.1 km and the predominance of land-based observation sites make it challenging to expand the sample size. In future studies, the challenge will be to increase the sample size by extending the period of RT simulations.

5. Aerosol and Cloud radiative forcing

The algorithm based on RT simulations with aerosols and cloud input, as described above, can be used to estimate aerosol and cloud radiative forcing, which are key factors in evaluating the impact of aerosols and clouds on the energy balance. Therefore, the L2 radiation product provides not only radiative flux and heating rates but also instantaneous radiative forcing due to aerosols and clouds. Figures 7 and 8 show the global distributions of the aerosol and cloud radiative forcing, respectively, as examples of the output from the algorithm. The radiative forcing shown was derived from the accumulation of instantaneous flux values with and without aerosols or clouds. Radiative forcing can be classified into SW and LW components at different levels: TOA, within the atmosphere (ATM), and at the SFC. Net radiative forcing is obtained by combining the SW and LW radiative forcing components.

The results in Figure 7 reveal the distinct characteristics of aerosol radiative forcing in the TOA and SFC. In the upper atmosphere, both SW and LW radiative forcing demonstrated varying responses to the presence of specific aerosols, resulting in either positive or negative radiative forcing. This finding emphasizes the influence of aerosol optical properties on the atmospheric radiative balance. The results in Figure 7 show that the spatial patterns of ATM and SFC are similar, and they are also similar to those of Oikawa et al. (2013). This can be attributed to the stronger influence of the underlying ground surface characteristics on the aerosol radiative forcing (Figure 7 (a), (d), and (g)). Aerosol radiative forcing plays an important role in the radiative balance of the atmosphere, and should be evaluated both at the surface and in the upper atmosphere. In the near future, the utilization of ATLID data from EarthCARE will be instrumental in enhancing the accuracy of aerosol radiative forcing assessments. For example, Nishizawa et al. (2019) demonstrated the potential of utilizing ATLID alone to estimate four additional aerosol types: WS, LA, DS, and SS. This expanded aerosol classification scheme provides valuable insights into the composition and optical properties of aerosols, enabling a more detailed and accurate assessment of aerosol radiative forcing. By incorporating these additional aerosol types into RT simulations in future research, we can enhance our understanding of the impact of different species of aerosols on Earth's radiative balance.

Figure 8 shows the radiative forcing due to clouds, showcasing distinct characteristics in terms of SW and LW radiation and their effects at both the TOA and the SFC. The SW component of cloud radiative forcing leads to cooling effects at both TOA and SFC, indicating that clouds reflect and scatter incoming solar radiation, reducing the amount of energy reaching the Earth's surface. Conversely, the LW component of cloud radiative forcing contributes to the heating effects at both the TOA and SFC as clouds absorb and re-emit LW radiation, trapping heat within the atmosphere. Furthermore, Figure 8 (d) shows that the SW component of the cloud radiative forcing generally induces heating within the ATM. This confirms that clouds have a warming effect on the atmospheric column by absorbing and redistributing the incoming solar radiation. In contrast, the LW component of cloud radiative forcing displayed distinct patterns that varied with latitude. At low- and mid-latitudes, LW forcing contributes to heating, implying that clouds enhance downward thermal radiation, thus warming the atmosphere in these regions (Figure 8 (e)). However, at high latitudes, LW forcing results in cooling, indicating that clouds reduce the downward thermal radiation, leading to a net cooling effect. These characteristics also confirm the spatial variability of LW cloud radiative forcing at TOA, ATM, and SFC and its influence on the Earth's energy balance at different height levels, as found in previous studies (e.g. Stephens et al. 2012). EarthCARE, with its advanced cloud particle detection capabilities of ATLID and Doppler CPR, is expected to enhance the accuracy of cloud radiative forcing estimates.

6. Conclusions

This paper describes the Level 2 (L2) algorithm for radiative flux and heating rate products generated by using the cloud and aerosol vertical information observed by CPR, ATLID, MSI, and BBR onboard the EarthCARE satellite. As a testbed before the launch of the EarthCARE satellite, A-Train data, particularly from CloudSat, CALIPSO, and MODIS, were used as inputs for the radiative transfer simulations, and the results were compared with CERES flux measurements at the TOA and with

BSRN measurement at the surface. Comparisons with flux observations revealed good agreement for downward longwave (LW) radiation, but significant discrepancies were observed for downward shortwave (SW) radiation, particularly in the presence of clouds. The validation results showed that the SW radiation fluxes in this study exhibited a positive bias but had smaller variability than the previous 2B-FLXHR-Lidar products. The LW fluxes demonstrated a similar level of accuracy to previous products in terms of bias and root mean square error (RMSE). The analysis was broken down into different cloud types and phases, suggesting that the positive bias in SW fluxes is likely attributable to an overestimation of the optical thickness of ice clouds used as input. In addition, we investigated the influence of spatial and temporal scales on radiative flux calculations. The increase in the scale led to a reduction in the RMSE and highlighted the importance of a larger sample size, particularly in the spatial dimension, to improve agreement with observations. Comparisons with ground-based observations from the BSRN showed a small bias in the SW radiative fluxes but an increased RMSE, potentially due to the limited number of ground-based measurements. These findings suggest the need for improved estimation of ice cloud properties to reduce the bias of SW radiative fluxes to achieve a more accurate radiation budget assessment and the cloud effect after the EarthCARE satellite is launched in 2024. The aerosol and cloud radiative forcing derived from this product can be provided in the form partitioned into Top of the Atmosphere (TOA), Atmosphere (ATM), and Surface (SFC). This capability will serve to quantitatively assess the effects of aerosols and clouds on the Earth's energy budget.

Data availability.

The MOD-Micro was provided by Prof. Takashi Y. Nakajima and Dr. Mirui Wang of Tokai University. Other JAXA products (CA-Aprop and CSCA-Micro) were obtained from the JAXA A-Train Product Monitor (https://www.eorc.jaxa.jp/EARTHCARE/research_product/ecare_monitor.html). The CloudSat data products of 2B-CWC-RO-R04 were provided by the CloudSat Data Processing Center at the CIRA/Colorado State University (https://www.cloudsat.cira.colostate.edu). MCD43C3 cells were obtained from the LP DAAC website (https://lpdaac.usgs.gov/products/mcd43c3v006/). CERES and GEOS-4,5 data included in the CCCM were obtained from NASA/LARC/SD/ASDC (https://doi.org/10.5067/AQUA/CERES/CCCM-FM3-MODIS-CAL-CS_L2.RELD1).

Author contributions.

AY performed the data analysis and the radiative transfer simulations. KS coordinated this work and obtained a funding. AY and KS produced the final manuscript draft. All authors reviewed the manuscript. MS, EJ, and HI developed the basic design of the radiation code. MS created Voronoi non-spherical tables. TMN provided feedback on the analysis methods as well as on the manuscript draft.

Competing interests.

The authors have no competing interests to declare.

Disclaimer.

Publisher's note: Copernicus Publications remains neutral with regard to jurisdictional claims in published maps and institutional affilia

tions.

395

Special issue statement.

This article is part of the special issue "EarthCARE Level 2 algorithms and data products." It is not associated with a conference.

Acknowledgements.

400 The authors would like to thank the members of the JAXA EarthCARE Science Team. We would like to thank Editage (www.editage.jp) for English language editing.

Financial support.

This study was funded by the Japanese Aerospace Exploration Agency (JAXA) EarthCARE Project (grant no.
405 24RT000226).

.

410
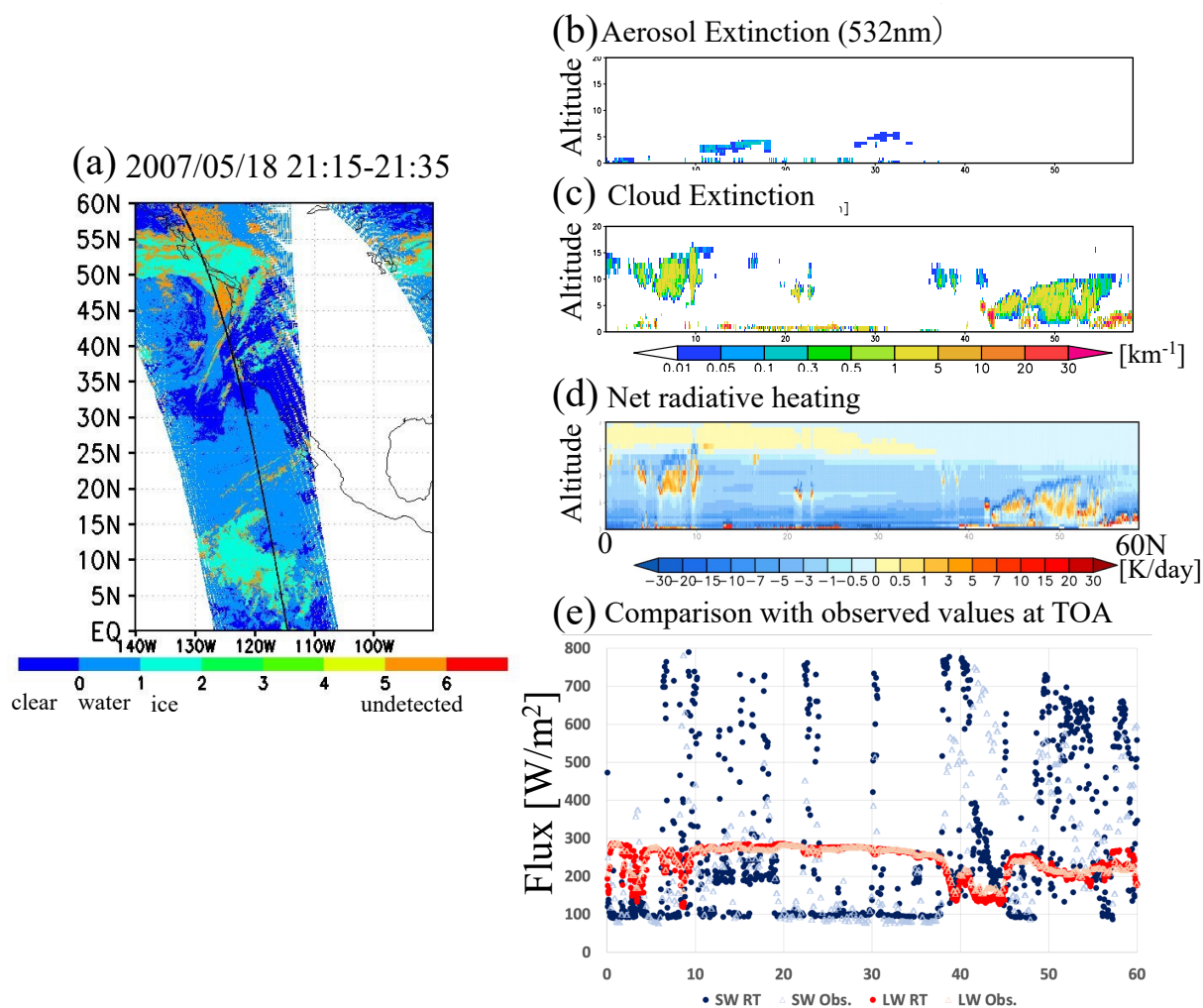
Figure 1.   Inputs and outputs from the flux algorithm, (a) Footprint of the A-Train is represented by the solid line, with cloud phase information from MODIS indicated in color, (b) input data for Aerosol Extinction, (c) Cloud Extinction (in km⁻¹), and (d) Net radiative heating (in K/day). (e) the SW fluxes in blue and LW fluxes in red resulting from the RT calculation at the TOA. Concurrently, observed SW fluxes (light blue) and LW fluxes (light red) from CERES at the TOA are juxtaposed for comparison.
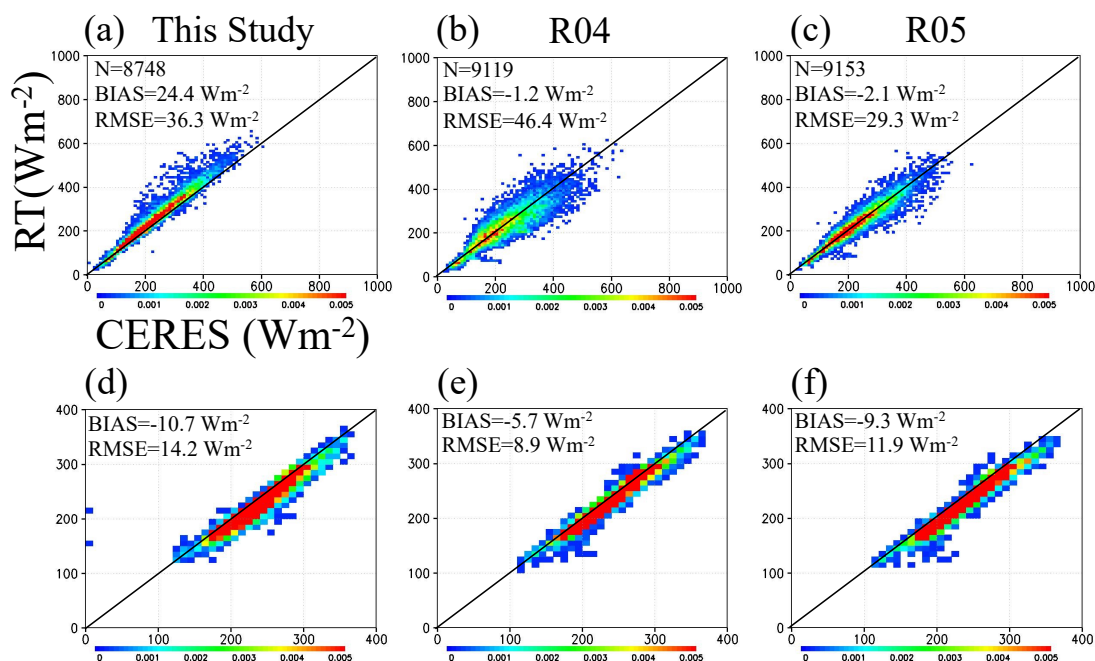
Figure 2. Comparison of monthly, 5°mean TOA flux RT calculations and CERES observations. (a.d) This study, (b,e) 2B-FLXHR-Lidar R04, and (c,f) 2B-FLXHR-Lidar R05, (a)-(c) out going SW radiation, and (d)-(f) out going LW radiation. The color represents frequency.

425
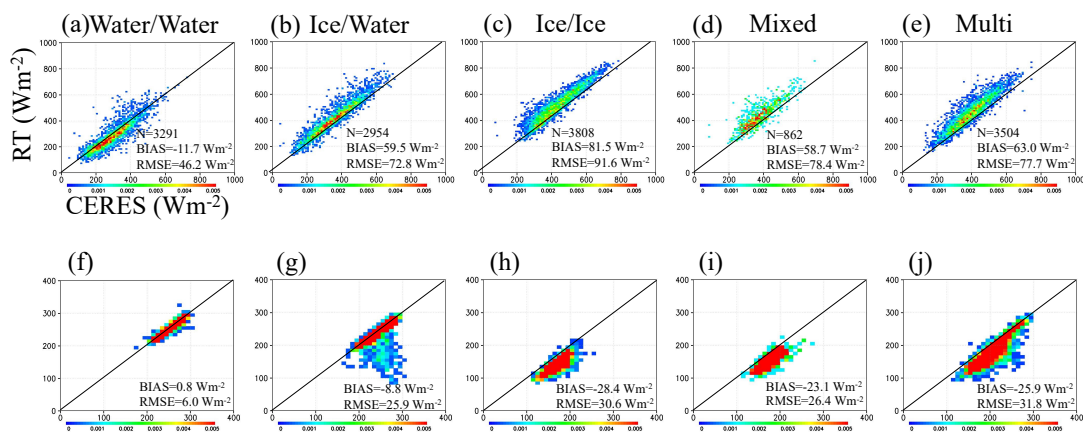
Figure 3. Same as Figure 2, but classified by cloud type. (a,f) water (CC)/water (MOD), (b,g) ice (CC)/water (MOD), (c,h) ice (CC)/ice (MOD), (d,i) mixed phase (CC), and (e,j) multi layered (CC) clouds. CC indicates cloud phase from

CloudSat/CALIPSO and MOD indicates cloud phase from MODIS. (a)-(e) out going SW radiation, and (f)-(j) out going LW
430 radiation. The color represents frequency.
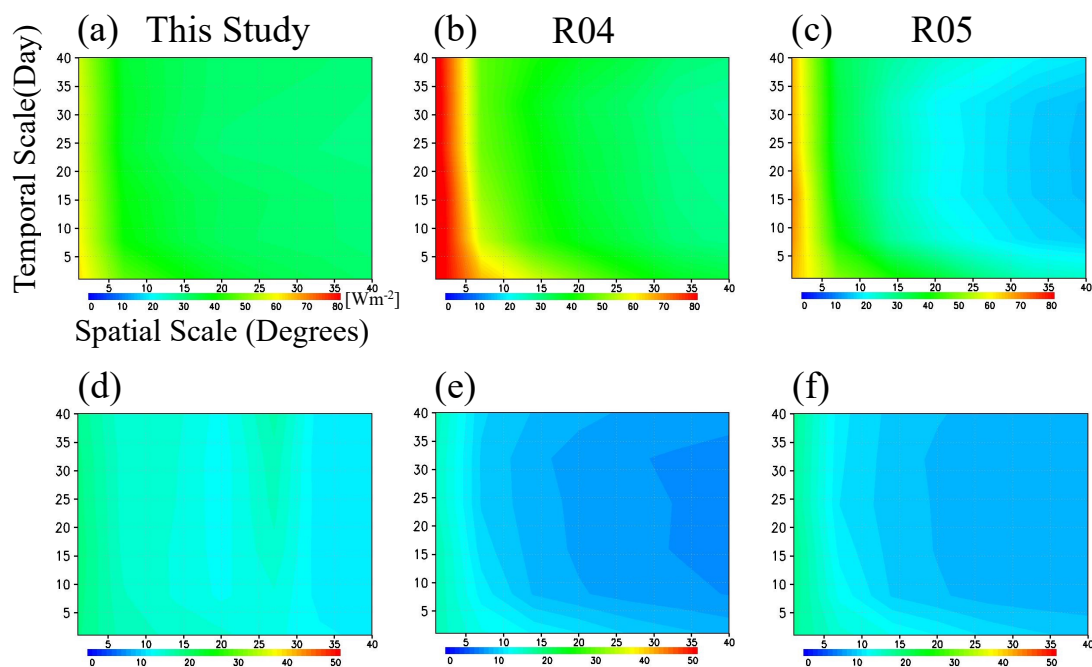
Figure 4. RMSE differences between TOA flux RT calculations and CERES observation on a variety of time and space scale.
(a.d) This study, (b,e) 2B-FLXHR-Lidar R04, and (c,f) 2B-FLXHR-Lidar R05, (a)-(c) out going SW radiation, and (d)-(f) out
going LW radiation. Color units are in Wm^{-2}.

435
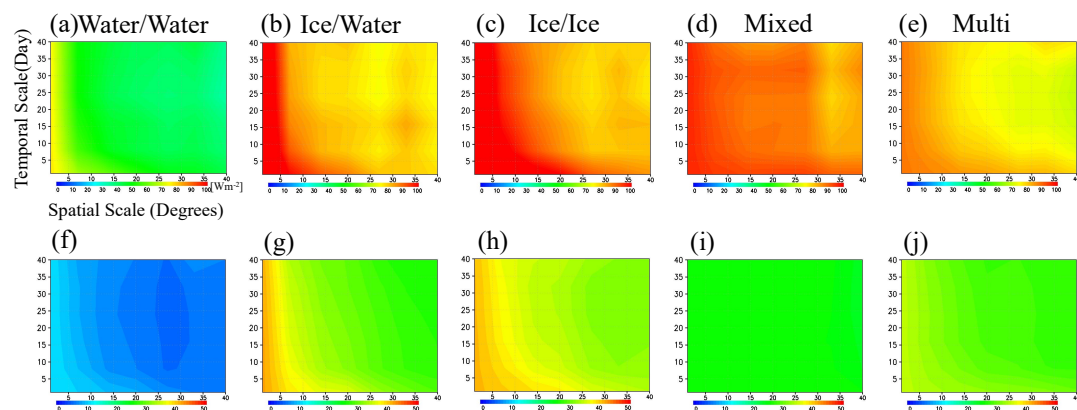
Figure 5. Same as Figure 4, but classified by cloud type. (a,f) water (CC)/water (MOD), (b,g) ice (CC)/water (MOD), (c,h) ice
(CC)/ice (MOD), (d,i) mixed phase (CC), and (e,j) multi layered (CC) clouds. CC indicates cloud phase from

CloudSat/CALIPSO and MOD indicates cloud phase from MODIS. (a)-(e) out going SW radiation, and (f)-(j) out going LW

440 radiation. Color units are in Wm^{-2}.
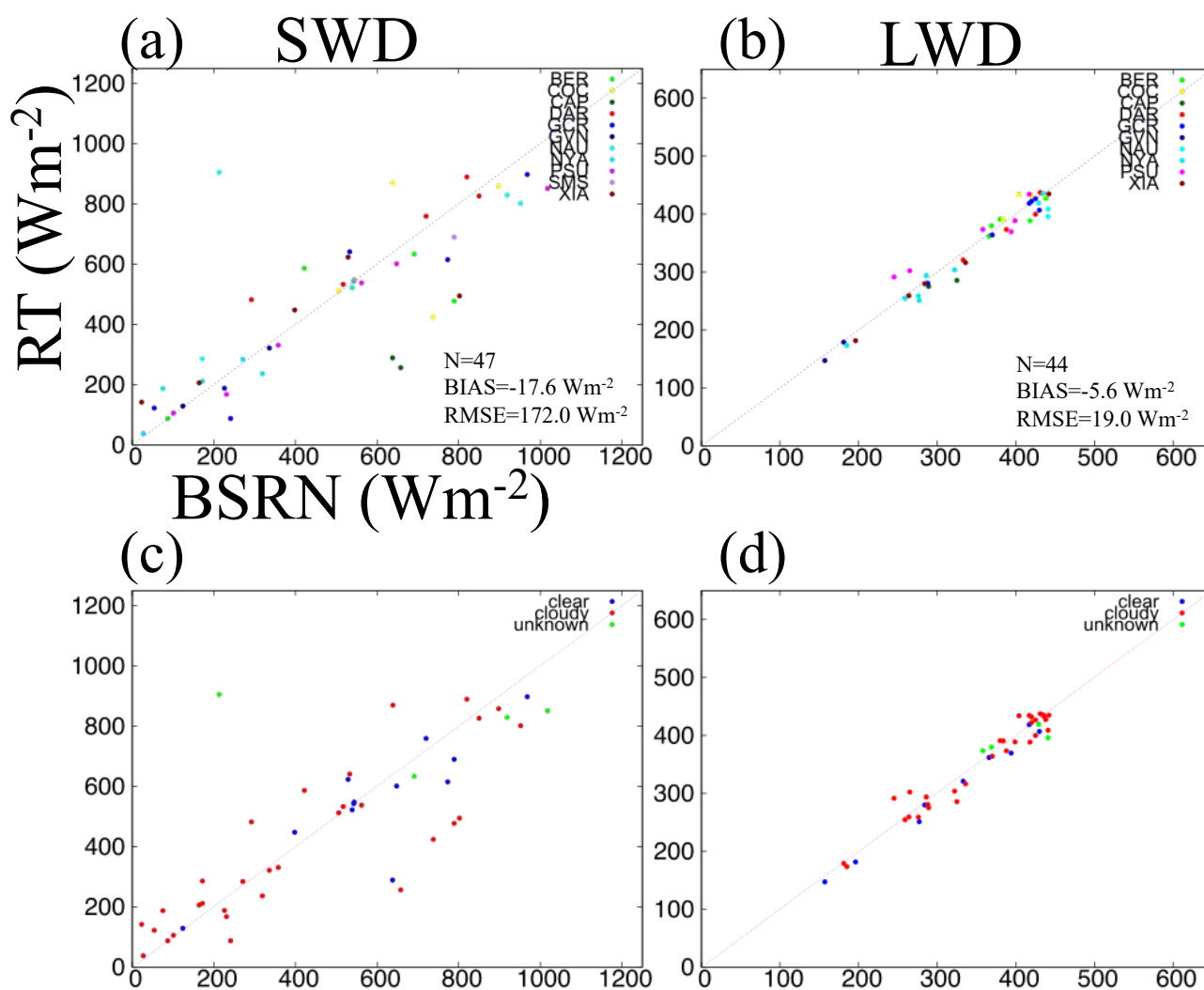
Figure 6. Comparative analysis between instantaneous surface flux RT calculations and observations obtained from the BSRN.

445 (a) and (b) illustrate the data points plotted according to observation locations, (c) and (d) categorize atmospheric conditions (blue: clear, red: cloudy, green: unknown). In detail, (a) and (c) focus on surface SW radiation, and (b) and (d) emphasize surface LW radiation. The names of BSRN stations are as follows: BER (Bermuda), COC (Cocos Island), CAP (Cape Baranova), DAR (Darwin), GCR (Goodwin Creek), GVN (Georg von Neumayer), NAU (Nauru Island), NYA (Ny-Ålesund), PSU (Rock Springs), SMS (São Martinho da Serra), and XIA (Xianghe).

450
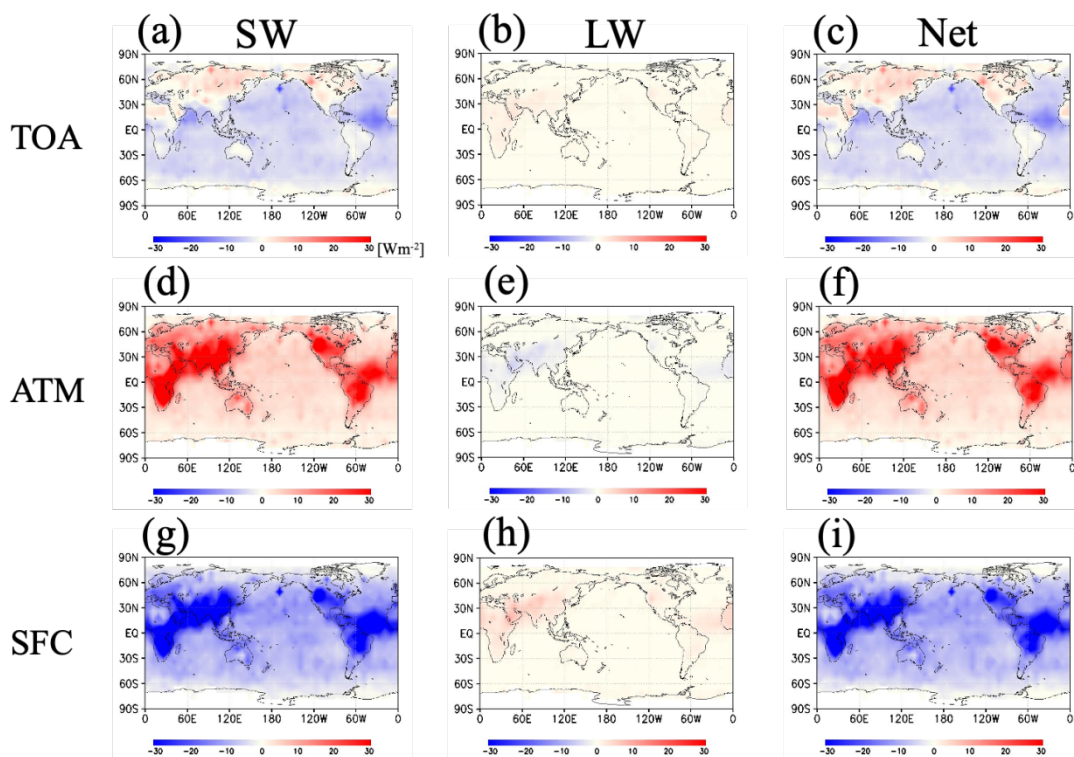
Figure 7. The 4-month average SW, LW, and net aerosol radiative effects under all-sky conditoins. In (a), (d), and (g), the focus is on SW effects, and (b), (e), and (h) provide insights into LW effects. (c), (f), and (i) depict Net effects, each corresponding to different atmospheric levels: (a-c) TOA, (d-f) ATM, and (g-i) SFC. Color units are in Wm^{-2}.

455
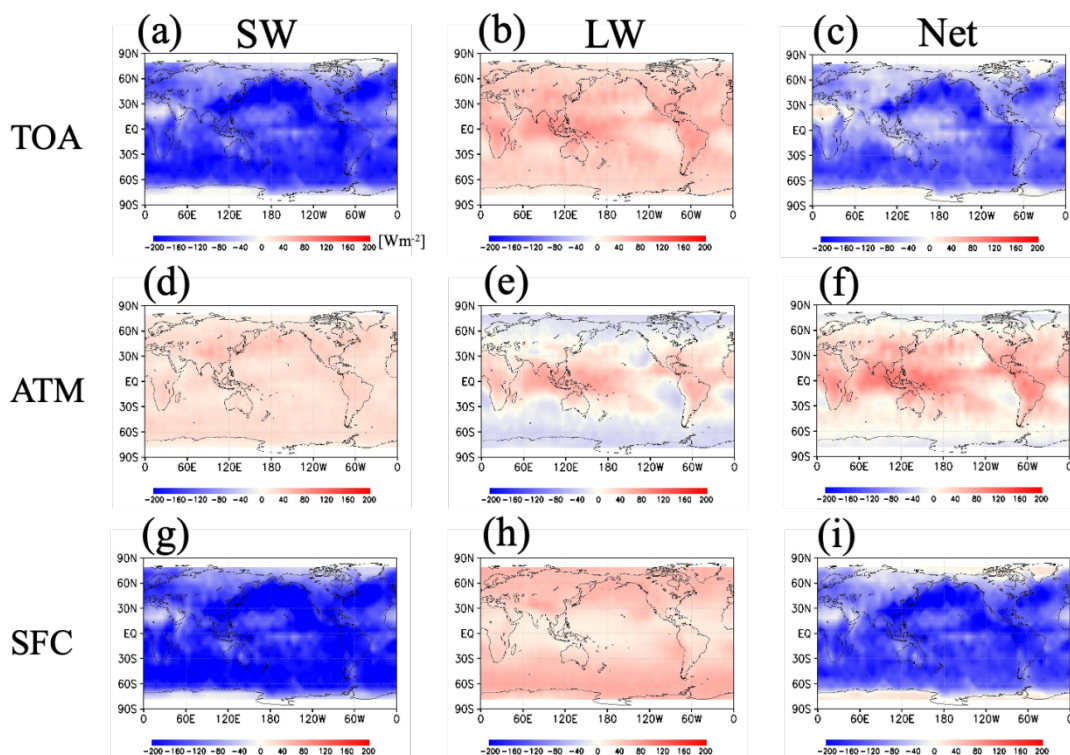
Figure 8. Same as Figure 7 but for cloud radiative effects. Color units are in Wm^{-2}.

References

460   Austin, R. T., A. J. Heymsfield, and G. L. Stephens,: Retrieval of ice cloud microphysical parameters using the CloudSat millimeter-wave radar and temperature, J. Geophys. Res., 114, D00A23, doi:10.1029/2008JD010049, 2009.

Barkstrom, B. R.: The Earth Radiation Budget Experiment (ERBE), Bull. Amer. Meteor. Soc., 65, 1170–1185, 1984.

465   Bloom, S., da Silva, A., and Dee D.: Documentation and validation of the Goddard Earth Observing System (GEOS) data assimilation system version 4, 1–187 pp, 2005.

Cole, J. N. S., Barker, H. W., Qu, Z., Villefranque, N., and Shephard, M. W. : Broadband radiative quantities for the EarthCARE mission: the ACM-COM and ACM-RT products, Atmos. Meas. Tech., 16, 4271–4288,
470   https://doi.org/10.5194/amt-16-4271-2023, 2023.

Fasullo, J. T., and Trenberth, K. E.: The annual cycle of the energy budget. Part I: Global mean and land-ocean exchanges, J. Climate, 21, 2297-2313, 2008a.

475 Fasullo, J. T., and Trenberth, K. E.: The annual cycle of the energy budget. Part II: Meridional structures and poleward ransports, J. Climate, 21, 2314-2326, 2008b.

Hartmann, D. L., and Short, D. A.: On the use of Earth radiation budget statistics for studies of clouds and climate, J. Atmos. Sci., 37, 1233–1250, 1980.
480
Henderson, D. S., L'ecuyer, T., Stephens, G., Partain, P., and Sekiguchi, M.: A multisensor perspective on the radiative impacts of clouds and aerosols, J. Appl. Meteor. Climatol., 52, 853-871, 2013.

Illingworth, A. J., Barker, H. W., Beljaars, A., Ceccaldi, M., Chepfer, H., Clerbaux, N., … Van Zadelhoff, G. J.: The
485 earthcare satellite : The next step forward in global measurements of clouds, aerosols, precipitation, and radiation. Bulletin of the American Meteorological Society, 96(8), 1311–1332. https://doi.org/105/BAMS-D-12-00227.1, 2015

Ishimoto, H., Zaizen, Y., Uchiyama, A., Masuda, K., Mano, Y.: Shape modeling of mineral dust particles for light-scattering calculations using the spatial Poisson–Voronoi tessellation, J. Quant. Spectrosc. Radiat. Transfer., 111, 2434-
490 2443, 2010.

Jiming L., Huang, J., Stamnes, K., Wang, T., Lv, Q., and Jin, H.: A global survey of cloud overlap based on CALIPSO and CloudSat measurements, Atmos. Chem. Phys., 15, 519–536, 2015, doi:10.5194/acp-15-519-2015.

495 Kato, S., and Coauthors.: Improvements of top-of-atmosphere and surface irradiance computations with CALIPSO-,CloudSat-, and MODIS-derived cloud and aerosol properties, J. Geophys. Res., 116, D19209, https://doi.org/10.1029/2011JD016050, 2011.

Kikuchi, M., Oki, R., Kubota, T., Yoshida, M., Hagihara, Y., Taka- hashi, C., Ohno, Y., Nishizawa, T., Nakajima, T. Y.,
500 Suzuki, K., Satoh, M., Okamoto, H., and Tomita, E.: Overview of Earth, Clouds, Aerosols and Radiation Explorer (EarthCARE) – Integrative Observation of Cloud and Aerosol and Their Ra- diative Effects on the Climate System, J. Remote Sens. Soc. Japan, 39, 181–196, https://doi.org/10.11440/rssj.39.181, 2019 (in Japanese).

Kudo, R., Higurashi, A., Oikawa, E., Fujikawa, M., Ishimoto, H., and Nishizawa, T.: Global 3-D distribution of aerosol

505   composition by synergistic use of CALIOP and MODIS observations, Atmos. Meas. Tech., 16, 3835–3863, https://doi.org/10.5194/amt-16-3835-2023, 2023.

Kyle, H. L., Ardanuy, P. E., and Hurley, E. J.: The Status of the Nimbus-7 Earth-Radiation-Budget Data Set, Bull. Amer. Meteor. Soc., 66, 1378-1388, 1985.

510

L'Ecuyer, T. S., Wood N. Haladay T., Stephens G. L., and Stackhouse Jr. P. W.: Impact of clouds on atmospheric heating based on the R04 CloudSat fluxes and heating rates data set, J. Geophys. Res., 113, D00A15, doi:10.1029/2008JD009951, 2008.

515   Liebmann, B., and Hartmann D. L.: Interannual variations of outgoing IR associated with tropical circulation changes during 1974–1978, J. Atmos. Sci., 39, 1153–1162, 1982.

Nakajima, T., Tsukamoto M., Tsushima Y., Numaguti A., and Kimura T.: Modeling of the radiative process in an atmospheric general circulation model, Appl. Opt., **39**, 4869-4878, doi:10.1364/AO.39.004869, 2000.

520

Nakajima, T. Y., and Nakajima T.: Wide-Area Determination of Cloud Microphysical Properties from NOAA AVHRR Measurements for FIRE and ASTEX Regions. Journal of the Atmospheric Sciences, 52(23), pp.4043-4059.DOI: 10.1175/1520-0469(1995)052<4043:WADOCM>2.0.CO;2, 1995

525   Nakajima, T. Y., Ishida, H., Nagao, T. M., Hori, M., Letu, H., Higuchi, R., Tamaru, N., Imoto, N., and Yamazaki, A.: Theoretical basis of the algorithms and early phase results of the GCOM-C (Shikisai) SGLI cloud products, Prog. Earth Planet. Sci., 6, 52, 2019.

Nishizawa, T., Okamoto, H., Sugimoto, N., Matsui, I., Shimizu, A., Aoki, K.: An algorithm that retrieves aerosol

530   properties from dual-wavelength polarized lidar measurements. J. Geophys. Res. Atmos., 112(D6), D06212, DOI: 10.1029/2006JD007435, 2007.

Nishizawa, T., Okamoto, H., Takemura, T., Sugimoto, N., Matsui, I., and Shimizu, A.: Aerosol retrieval from two-wavelength backscatter and one-wavelength polarization lidar measurement taken during the MR01K02 cruise of the

535 R/V Mirai and evaluation of a global aerosol transport model, J. Geophys. Res. Atmos., 113(D21), D21201. DOI: 10.1029/2007JD009640, 2008.

Nishizawa, T., Sugimoto, N., Matsui, I, Shimizu, A., and Okamoto, H.: Algorithms to retrieve optical properties of three component aerosols from two-wavelength backscatter and one-wavelength polarization lidar measurements considering
540 nonsphericity of dust, J. Quant. Spectrosc. Radiat. Transfer., 112, 254-267, 2011.

Nishizawa, T., Kudo, R., Higurashi, A., Oikawa, E., and Okamoto, H.: Aerosol and Cloud Retrieval Algorithms Using EarthCARE Satellite-Borne Lidar Data, J. Rem. Sens. Soc. Jap., 39, 215-224, 2019. (in Japanese)

545 Ohmura, A., Dutton, E., Forgan, B., Frohlich, C., Gilgen, H., Hegne, H., Heimo, A., Konig-Langlo, G., McArthur, B., Muller, G., Philipona, R., Whitlock, C., Dehne, K., and Wild M.: Baseline Surface Radiation Network (BSRN/WCRP): New precision radiometry for climate change research. Bull. Amer. Meteor. Soc., 79, 2115–2136, 1996.

Oikawa, E., Nakajima, T., Inoue, T., and Winker, D.: A study of the shortwave direct aerosol forcing using
550 ESSP/CALIPSO observation and GCM simulation, J. Geophys. Res. Atmos., 118, 3687–3708. https://doi.org/10.1002/jgrd.50227, 2013

Okamoto, H., Sato K., and Hagihara Y.: Global analysis of ice microphysics from CloudSat and CALIPSO: Incorporation of specular reflection in lidar signals, J. Geophys. Res. Atmos., 115(D22), D22209, DOI:
555 10.1029/2009JD013383, 2010.

Oreopoulos, L., Cho N., Lee, D.: New insights about cloud vertical structure from CloudSat and CALIPSO observations, J. Geophys. Res. Atmos., 122, 17, 9280-9300, 2017.

560 Platnick, S., and Coauthors: The MODIS cloud optical and microphysical products: Collection 6 updates and examples from Terra and Aqua. IEEE Trans. Geosci. Remote Sens., 55, 502–525, 2017.

Rienecker, M. M., Suarez, M. J. and co-authors,: The GEOS-5 Data Assimilation System – Documentation of Versions 5.0.1, 5.1.0, and 5.2.0. Technical Report Series on Global Modeling and Data Assimilation, 27,
565 NASA/TM−2008−104606, National Aeronautics and Space Administration (available at: http://gmao.gsfc.nasa.gov/pubs/docs/Rienecker369.pdf), 2008.

Roesch, A., Schaaf, C., and Gao, F.: Use of Moderate-Resolution Imaging Spectroradiometer bidirectional reflectance distribution function products to enhance simulated surface albedos, J. Geophys. Res., 109, D12105. https://doi.org/10.1029/2004JD004552, 2004.

Rothman, L. S., Jacquemart, D., Barbe, A., Benner, D. C., Birk, M., Brown, L. R.,… Wagner, G.: The HITRAN 2004 molecular spectroscopic database, J. Quant. Spectrosc. Radiat. Transfer, 96, 139-204, doi:10.1016/j.jqsrt.2004.10.008, 2005.

Sassen, K., Wang, Z., Liu, D.: Global distribution of cirrus clouds from CloudSat/Cloud-Aerosol Lidar and Infrared Pathfinder Satellite Observations (CALIPSO) measurements, J. Ggeophys. Res., 113, D00A12, doi:10.1029/2008JD009972, 2008.

Sato, K., and Okamoto, H.: Refinement of global ice microphysics using spaceborne active sensors. J. Geophys. Res. Atmos., 116(D20), D20202, DOI: 10.1029/2011JD015885, 2011.

Schaaf, C. B., Gao, F., Strahler, A. H., Lucht, W., Li, X., Tsang, T.,…Roy, D.: First operational BRDF, albedo nadir reflectance products from MODIS, Remote. Sens. Environ., 83(1-2), 135–148. https://doi.org/10.1016/S0034-4257(02)00091-3, 2002.

Sekiguchi, M., and Nakaima T.: A k-distribution-based radiation code and its computational optimization for an atmospheric general circulation model, J. Quant. Spectrosc. Radiat. Transfer, **109**, 2779-2793, 2008

Stephens, G. L., Vane, D. G, Tanelli, S., … Marchand, R.: CloudSat mission: Performance and early science after the first year of operation. J. Geophys. Res., 113, D00A18, https://doi.org/10.1029/2008JD009982, 2008.

Stephens, G. L., Li, J., Wild, M., Clayson, C. A., Loeb, N., Kato, S., … Andrews, T.: An update on Earth's energy balance in light of the latest global observations, Nature Geosci., 5(10), 691–696. https://doi.org/10.1038/ngeo1580, 2012.

Wang, M., Nakajima, T. Y., Roh, W., Satoh, M., Suzuki, K., Kubota, T., and Yoshida, M.: Evaluation of the spectral misalignment on the Earth Clouds, Aerosols and Radiation Explorer/multi-spectral imager cloud product. Atmos. Meas. Tech., 16, 603–623, https://doi.org/10.5194/amt-16-603-2023, 2023.

600

Wielicki, B. A., Barkstrom, B. R., Harrison, E. F., Lee III R. B., Smith, G. L., and Cooper, J. R.: Clouds and the Earth's Radiant Energy System (CERES): An earth observing system, Bull. Am. Meteorol. Soc., 72, 853–868, 1996.

Winker, D. M., Pelon, J., Coakley, J. A. Jr., Ackerman, S. A., Charlson, R. J., Colarco, P. R.,…Wielicki, B. A.: The
605 CALIPSO mission: A global 3D view of aerosols and clouds. Bulletin of the American Meteorological Society, 91, 1211–1230, https://doi.org/10.1175/2010BAMS3009.1, 2010.